

# Development of Microstructure and Mechanical Properties of TiAl6V4 Processed by Wire and Arc Additive Manufacturing

Daniel Elitzer, Stefanie Jäger, Clara Höll, Daniel Baier, Rosa Varga, Michael F. Zaeh, Mathias Göken, and Heinz-Werner Höppel\*

Wire and arc additive manufacturing (WAAM) has the potential to significantly reduce material waste due to the milling of components made of TiAl6V4 (Ti-64). To keep up with the market development, this resource-efficient technology is becoming increasingly important to achieve climate policy goals. Therefore, this study not only focuses on the influence of different process parameters, such as torch and wire feed speed, but also different gas mixtures on the microstructure and related mechanical properties, as well as on the scalability by investigating single- to multilayer welded structures. The wire feed speed is found to have a major influence on the geometry and mechanical properties. The use of different process gases, i.e., argon (Ar), helium (He), and a mixture of 70% He and 30% Ar neither significantly affect the microstructure nor the mechanical properties. It is also found that a solution heat treatment followed by an annealing step degrades mechanical properties, while an ordinary stress-relief heat treatment leads to improved mechanical properties. It is shown that by adapting WAAM process and heat treatment parameters, mechanical properties of additively produced specimens can be achieved, which are fully comparable to milled components.

## 1. Introduction


One of the most commonly used alloys in the aerospace industry is the titanium alloy TiAl6V4 (Ti-64), accounting for 56%<sup>[1–4]</sup> of the world's total titanium production. Pure titanium shows an allotropic phase transformation. In addition to the hexagonal close-packed  $\alpha$ -phase, which exists at room temperature, the body-centered cubic  $\beta$ -phase is stable at higher temperatures of  $\approx 882^\circ\text{C}$ . The addition of aluminum stabilizes the  $\alpha$ -phase, while the  $\beta$ -phase is stabilized by adding vanadium. Different heat treatment processes can be utilized to achieve various microstructures and thus different property spectra. In combination with a low density of  $\approx 4.5\text{ g cm}^{-3}$ , this results in outstanding mechanical properties like a highly specific strength paired with a high ductility which can be set for the respective application.<sup>[1,5]</sup>

Structural parts made of Ti-64 are often used in highly stressed areas of an aircraft. Currently, these components are milled from solid-rolled semifinished products, resulting in up to 95%<sup>[6,7]</sup> of the material being machined. Given the high oxygen affinity of titanium alloys, chips cannot remain in the material cycle and have to be disposed of.<sup>[5,8–11]</sup> With regard to ecological aspects and to be able to achieve climate policy goals, a more eco-efficient manufacturing process for structural components is desirable. In addition, the demand for Ti-64 structural components for aircraft is expected to rise, thus, this problem will become increasingly important. Near-net-shape production of these structural components is a promising approach to solve this problem.<sup>[12–19]</sup> Many of the standard additive manufacturing processes, e.g., laser powder bed fusion or electron beam melting, allow the fabrication of more complex structures due to the powder feedstock and a small diameter of heat input.<sup>[20–22]</sup> However, these techniques have slow build-up rates and are often also restricted to smaller part sizes, which make these techniques inefficient for the need of serial production for larger aviation parts. Additive manufacturing based on existing knowledge of arc welding techniques, such as wire and arc additive manufacturing (WAAM), is not only capable of reducing machining time and energy consumption, but also

D. Elitzer, S. Jäger, C. Höll, M. Göken, H.-W. Höppel  
Department of Materials Science & Engineering  
Institute I: General Materials Properties  
Friedrich-Alexander-Universität Erlangen-Nürnberg FAU  
Martensstrasse 5, 91058 Erlangen, Germany  
E-mail: hwe.hoepfel@fau.de

D. Baier, M. F. Zaeh  
School of Engineering and Design  
Institute for Machine Tools and Industrial Management  
Technical University of Munich (TUM)  
Boltzmannstrasse 15, 85748 Garching, Germany

R. Varga  
AMAG Components Übersee GmbH  
Gewerbestr. 12-14, 83236 Übersee, Germany

 The ORCID identification number(s) for the author(s) of this article can be found under <https://doi.org/10.1002/adem.202201025>.

© 2022 The Authors. Advanced Engineering Materials published by Wiley-VCH GmbH. This is an open access article under the terms of the Creative Commons Attribution License, which permits use, distribution and reproduction in any medium, provided the original work is properly cited.

DOI: 10.1002/adem.202201025

significantly decreasing material loss.<sup>[5,6,23–27]</sup> Depending on the component, the degree of metal removal can be reduced from 98% to 7–20%.<sup>[6]</sup>

Various groups have already demonstrated the potential of the WAAM process and shown possibilities to produce more complex and larger structures.<sup>[28–34]</sup> However, a significant challenge remains the scalability of the process from small to larger structures. While process parameters were still able to produce high-quality structures for experimental geometries, it was found in our studies that they were no longer able to produce high-quality results for more complex geometries. Therefore, this article focuses on the development of microstructural features of additively manufactured specimens via wire (WAAM-ed samples) and the scalability of used parameters, starting with a wire analysis, and proceeding to create single- and multibead specimens to more complex structures, like T-joints. Analyzing the early stages of WAAM-ed samples provides critical information about microstructural and mechanical development in the substrates heat-affected zone (HAZ) up to the first layers of the additively manufactured material, which is crucial for components exposed to cyclic loading.

In addition, the resulting mechanical properties are analyzed along the process chain and the influence of different welding power sources and process gases is evaluated.

Experimental Section Within the scope of this work, experimental parameter studies were conducted to qualify a stable process window. Investigations were carried out on single-layer and multilayer specimens. As part of a statistically designed experimental plan (EP), welding-specific process variables, such as torch and wire feed speed, as well as arc correction factors to determine a stable process window and environmental parameters were varied. Thus, the process gas composition was varied to investigate the possibility of extending the stable process window.

Single-layer, multilayer wall-shaped, and complex parts using Ti-64 wires from E. Wagener GmbH, Weissach-Flacht, were manufactured, see **Figure 1**.

## 2. Specimen Manufacturing

Titanium has a high affinity for oxygen absorption at elevated temperatures. This leads to welding defects and embrittlement, which reduce the quality of the component in case of stronger oxygen contamination. To decrease the absorption of oxygen during the welding process, an inert gas atmosphere was used. For this purpose, a welding enclosure filled with argon 4.6 from Huntingdon fusion techniques was used.

The samples analyzed for this work were produced on two different machines. The system at AMAG components Übersee GmbH was a portal axis-based Gefertec arc605 (GT) AM cell. The system at the Technical University of Munich (TUM) was robot based. It consisted of a robot system from Kuka AG (KR15/2) and a welding power source from Fronius International GmbH (CMT Advanced 4000R). Both WAAM machines used Fronius' cold metal transfer (CMT) process. CMT is characterized by a pulsating wire electrode.<sup>[35]</sup> By mechanically depositing the weld metal droplet without electromagnetic forces, the energy input can be reduced, and therefore, the penetration depth of the arc (burn-in depth) is also lower compared to conventional metal inert gas welding (MIG) welding processes. This increases the build-up rate and reduces the thermomechanical residual stresses that result in component distortion. Furthermore, the use of correction factors, i.e., arc length and dynamic correction, increases the stability of the arc, and process termination due to spattering or interrupted arcs are minimized. The combination of MIG and CMT also improves the esthetics of the weld bead.<sup>[35,36]</sup>

Multilayer wall-shaped samples were produced using a pendulum motion.

The input variables considered as process parameters in the Design of Experiments are shown in **Table 1**, which also gives the values of the applied correction factors. In these first build jobs, the effect of the process gases argon (Ar) and helium (He) on the welding properties were compared at different travel speeds ( $v_{TS}$ ) and wire feed speeds ( $v_{WFS}$ ).

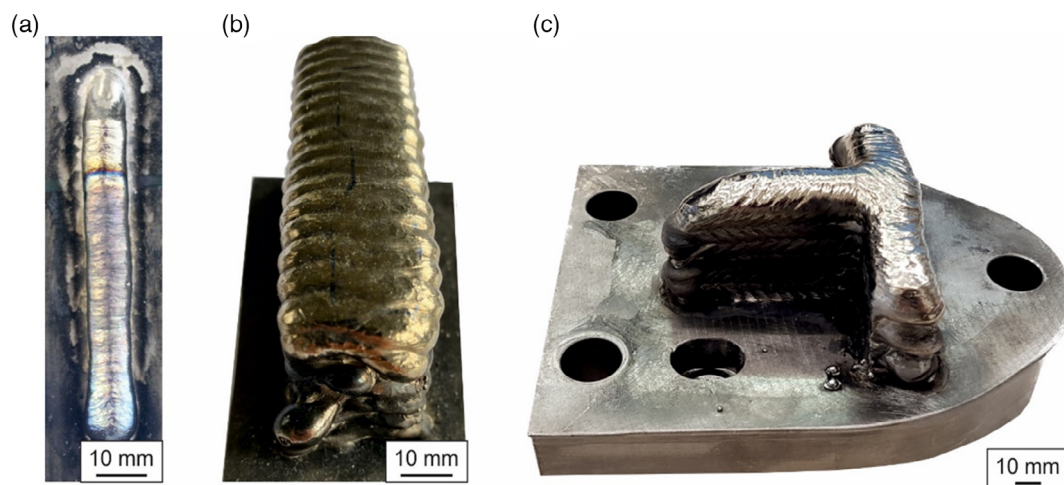


**Figure 1.** Overview of: a) single-, b) multilayer, and c) complex specimens (T-joints) investigated.

**Table 1.** Process parameters for single-bead study comparing different process gases.

	$V_{TS}$ [mm min <sup>-1</sup> ]	$V_{WFS}$ [m min <sup>-1</sup> ]	Correction Factors		Shielding Gas
			Arc [%]	Dynamic [%]	
Build Job 1	133	4	-30	-5	Argon
	160		-15	-2,5	
	200		0	0	
	267		15	2,5	
	400		30	5	
Build Job 2	80	1,5	20	0	Helium
	200	4,5			
	300	11			
	400				
Build Job 4	66	4	30	5	Helium
	82	5			
	99	6			
T-joints	87	8	-10	0	Argon
	112	9			
	137	11			
	161				

The knowledge gained from the multilayer build jobs was used to derive parameters with which more complex geometries were manufactured. For the production of these T-joints, two different parameter sets were used, consisting of the wall parameter (black line in **Figure 2**) and a parameter to produce the connection between the two walls (red line in **Figure 2**). Two promising welding parameters were chosen to build the walls for this study. To investigate the influence of the travel and wire feed speed on the bonding capabilities, many different connection parameters were investigated, but only those with a slower torch speed compared to the wall parameter are presented in this article. The travel speeds were 87, 112, and 137 mm min<sup>-1</sup> with a wire feed speed of 8, 9, and 11 m min<sup>-1</sup>, respectively.

For the processing of multilayered Ti-64 specimens, different inert process gases were also used in the experiments. The influence of the process gas on the component properties was

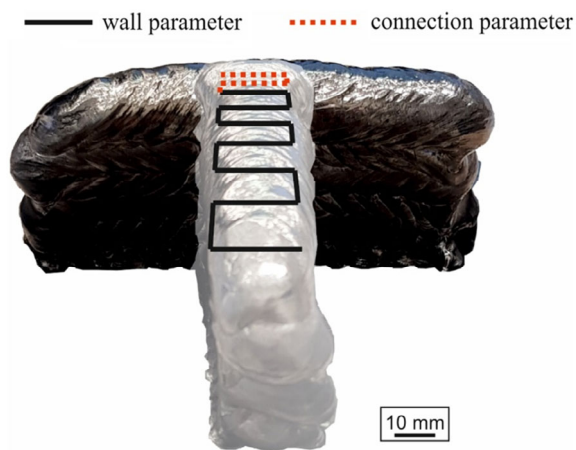


**Figure 2.** Schematic illustration of different parameter sets to achieve a nonporous connection in the T-joints.

**Table 2.** Composition of the wires used for the robot-axis-based welding system at technical university of Munich (TUM) and the portal-axis-based welding system at AMAG components Übersee GmbH (GT).

Composition in wt%	Ti	Al	V	Fe	C	N	O	H
TUM	bal.	6.3	3.96	0.14	0.007	0.006	0.153	0.004
GT	bal.	6.2	3.89	0.17	0.023	0.006	0.15	0.0004

investigated using Ar and He from Linde GmbH, Pullach. The process parameters were adjusted due to the different process windows caused by the gas.

The wire diameter of the electrode to be welded was 1.2 mm. The wires were certified according to ASTM E407 and ASTM E1447 and tested for microstructure properties and oxygen contamination. The chemical composition of the wires can be found in **Table 2**.

### 3. Macro- and Microscopy

After fabrication, all parts were cut vertically, using corundum cut-off wheels, and examined concerning their macrostructure. The specimens were ground and polished using grinding paper and a 1 µm diamond suspension. The microstructure was visualized with Kroll etchant and examined with a Zeiss “Axio” light microscope and a Wild Heerbrugg M420 stereo microscope. Further samples were taken in both vertical and horizontal directions to investigate any directional dependence of the microstructure. These analyses were carried out using a Zeiss CrossBeam 1540 EsB (SEM) combined with an Oxford INCA Energy 350 EDX system to study chemical anomalies. Grain orientation studies were performed using an Oxford Nordlys II system (EBSD).

### 4. Heat Treatment and Process Gases

In addition to the as-built condition, samples were also examined after different heat treatments. Stress-relief annealing (SR) was performed at 600 °C for 4 h. A two-stage solution heat treatment and annealing (STA) were performed at 1200 °C with cooling to 843 °C for 2 h, respectively. All heat treatments were performed in vacuum (10<sup>-5</sup> mbar) followed by furnace cooling.

### 5. Mechanical Testing

Hardness measurements and compression tests were carried out for mechanical characterization. For hardness measurements, a Vickers tip geometry was used on a Leco M-400-G with a holding time of 10 s. Compression tests were performed at a strain rate of 10<sup>-3</sup> s<sup>-1</sup> on an Instron 4505 equipped with a Hegewald and Peschke control system.

### 6. Results and Discussion

Additive manufacturing starts with a base material that is melted by energy input and thus maps the final component geometry

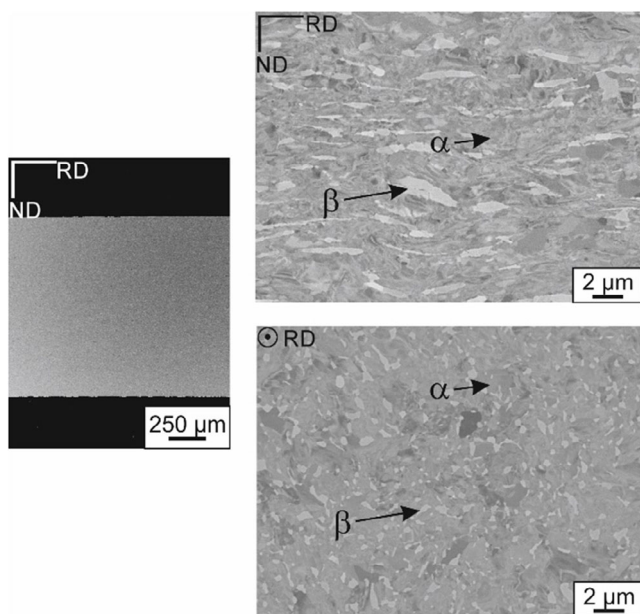


**Figure 3.** Microstructural images of Ti-64 wire material before AM in different views along the rolling direction (RD) and transversal.

layer by layer. The wire material shows an  $\alpha + \beta$  microstructure elongated in the rolling direction (RD), which is caused by the wire drawing process, see **Figure 3**.

Parallel to the rolling direction, the microstructure displays a fine globular structure. During manufacturing, smolder evaporates. The EDS analyses of smoldering revealed a high amount of aluminum about 58–60%. It is commonly known that the alloying elements with a low melting point and high vapor pressure, compared to the rest of the alloy, tend to evaporate during additive manufacturing.<sup>[37–39]</sup> Therefore, further, EDS analyses of the WAAM part were performed. **Figure 4** shows the impact of element burn-off occurring in WAAM.

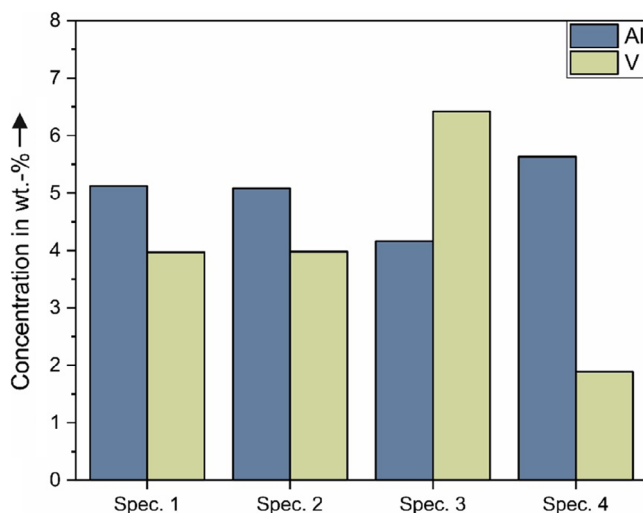


**Figure 4.** Chemical composition by the EDS analyses of wire and arc additive manufacturing (WAAM)-ed specimens.

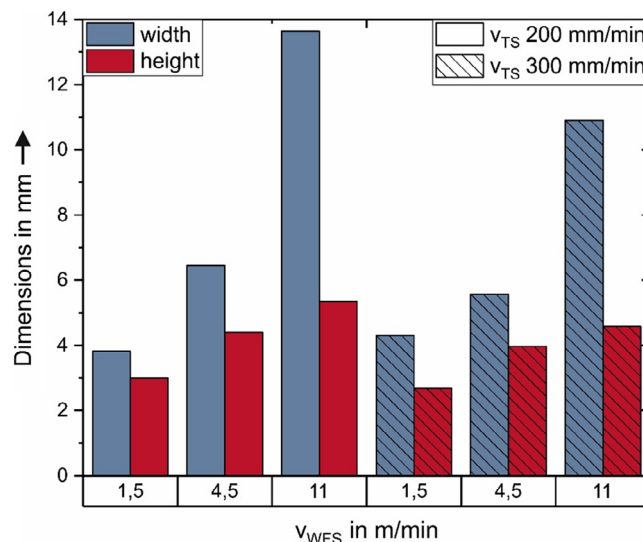


**Figure 5.** Influence of the process parameters travel speed ( $v_{TS}$ ) and wire feed speed ( $v_{WFS}$ ) on geometry.

The concentration of titanium was found to be about 91 wt%. The concentration of aluminum in the alloy decreases slightly due to the high energy input of the arc, as can be seen in spectrum (Spec.) 1 and 2. Point measurements in lamellar (Spec. 4) and interlamellar regions (Spec. 3) also indicate the element segregation of the two phases, however, for a more detailed EDS analysis TEM investigations have to be performed. Another point worth mentioning is the effect of the process parameters on the geometry. **Figure 5** shows the resulting sample dimensions versus travel speeds  $v_{TS}$  of 200 and 300  $\text{mm min}^{-1}$ , and different wire feed speeds  $v_{WFS}$  ranging from 1.5 to 11  $\text{m min}^{-1}$ .

It can be seen that regardless of  $v_{TS}$ , with increasing wire feed speed, the width of the bead increases more than the height.

An additional increase in  $v_{TS}$  results in a higher cooling rate and thus in a decreasing weld pool width and depth. These influences must be kept in mind when evaluating the microstructures.

## 7. Single-Layer Specimens

**Figure 6** compares the investigated processes, Puls and CMT, and the influence of the process gas He and Ar.

From the microscopic images (Figure 6a,d,g) of the samples produced at a travel speed of 200  $\text{mm min}^{-1}$ , it can be seen that CMT-argon generates an increased material deposition. The additional wire movement of the CMT process also decreases the burn-in depth of the arc, and therefore, the distortion of the base plate slightly.

The formerly elongated and globular  $\alpha + \beta$  microstructure of the wire transforms into a lamellar microstructure, regardless of the process or the parameters, Figure 6. Due to the cold base plate, the melt pool cools rapidly, resulting in this microstructure.

Generally, the increased  $v_{TS}$  results in finer  $\alpha$ -lamellae, caused by a smaller melt pool width, which leads to higher cooling rates.

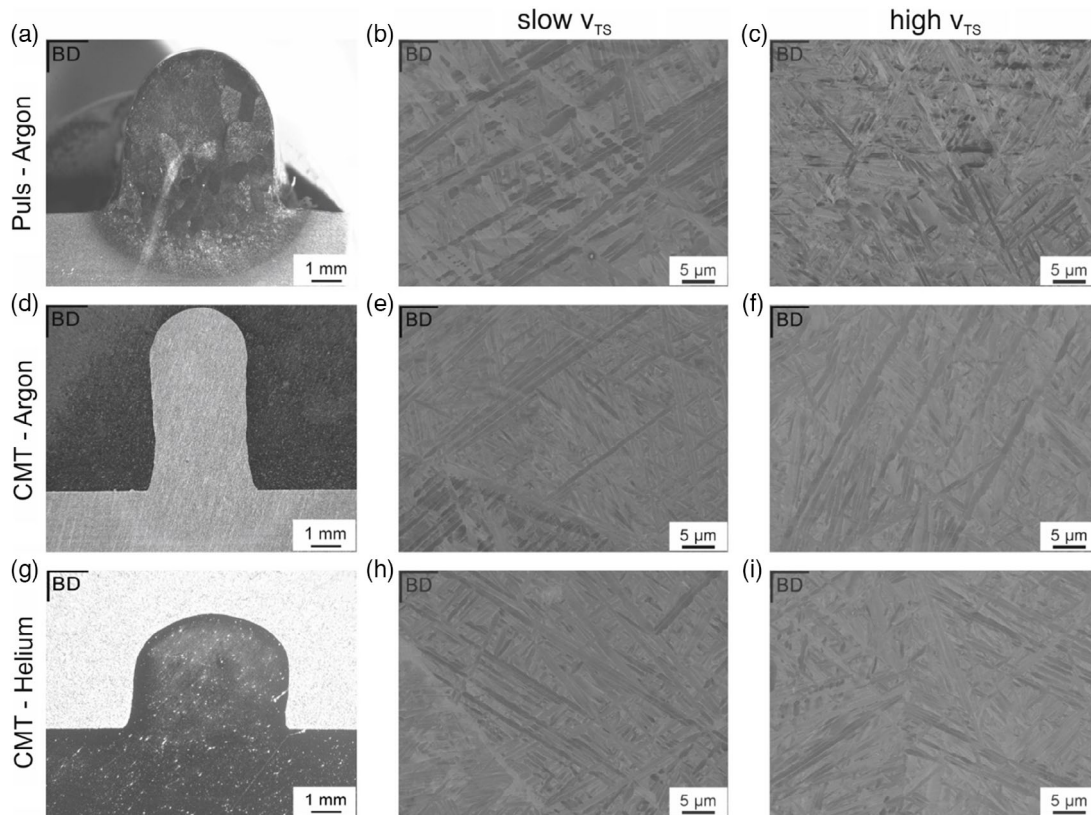


**Figure 6.** Influence of different welding modes (CMT/Puls) and process gases (Argon/Helium) on the macro- and microstructure. a,d,g): Macrostructure of the single layer wall (cross-section) for a) Puls-Argon, d) CMT-Argon and g) CMT-Helium with b,e,h): related microstructures for a slow torch speed and c,f,i): for high welding speeds.

Qualitatively the obtained Widmanstätten microstructure is not affected by the welding mode.

The use of helium as an inert process gas led to a stabilization of the arc, but no change in the microstructure was observed. To figure out potential differences in the microstructure of the lamellar spacing, a more significant variation in  $v_{TS}$  was analyzed, **Figure 7**.

Although the lamellar spacing is high for slow  $v_{TS}$  for a medium range of  $v_{TS}$ , no differences are visible within the scatter of the data. As a result of the increased heat transfer coefficient of helium, cooling by convection is faster compared to argon at constant parameters. One would like to assume a small effect of the welding mode and process gas on the lamellar spacing, but within the scatter of the data, no distinct differences can be stated. Instead, the microstructures of all examined specimens do not show any pronounced evidence of the influence of the inert gas on the lamellar spacing. The reason for this may be a change in the weld pool geometry. Specimens welded in a helium atmosphere are wider and show a significantly smaller height than specimens processed with argon (Figure 6d,g). The improved thermal conductivity, however, is balanced out by a reduced cooling rate caused by the lower surface area, which also results in comparable microstructures. It was not possible to produce medium- and slow-speed samples using helium as a process gas because the specimens oxidized or spatter formed

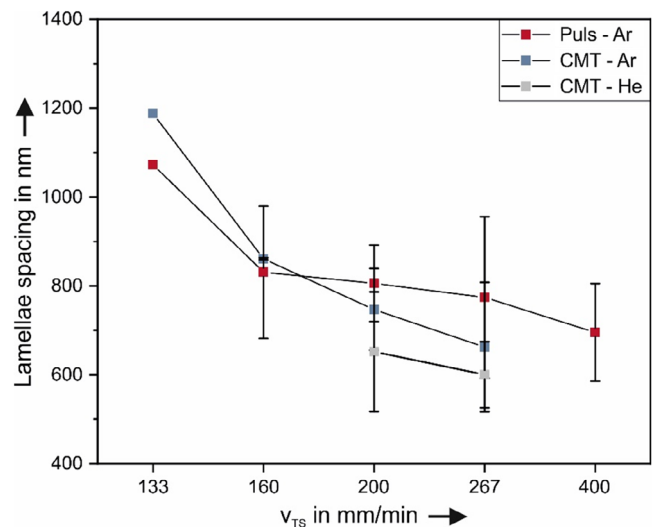


**Figure 7.** Lamellae spacing as a function of  $v_{TS}$  with a constant  $v_{WFS}$  of  $4 \text{ m min}^{-1}$ .

due to a stalling inert gas atmosphere. This inhomogeneous gas atmosphere can be explained by the low density of helium, which increases the difficulty of a uniform gas flow. Thus, this can be assumed to be a process limit. Hardness measurement

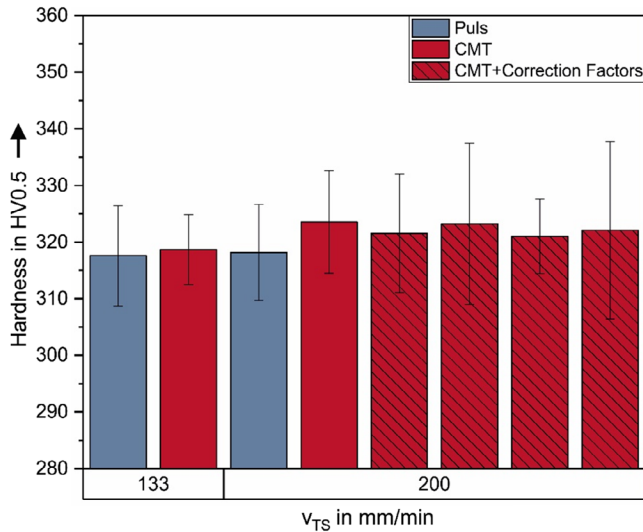


**Figure 8.** Hardness of single-layer material produced with argon depending on  $v_{TS}$  and correction factors.

showed a slight increase with higher  $v_{TS}$ . **Figure 8** also reveals that the use of correction factors to stabilize the arc during the welding process has a negligible influence on the hardness.

Pulsed processes (blue columns) show comparable properties to CMT, however, the distortion was higher. Based on this and the above-presented findings, all multilayer specimens were subsequently produced only using Fronius' CMT technology.

## 8. Multilayer Material

Based on the results of the single-layer tests, a test matrix was set up for multilayer and more complex components. A typical macrostructure of WAAM-ed Ti-64 is shown in **Figure 9a**. It consists of three main parts: the base plate, the connection, and the weld itself. The high energy input of the welding process in the first layer leads to a partial remelting of the baseplate, which produces a cohesive connection to the weld seam.

Since the base plate is at room temperature, a high cooling rate is achieved in the HAZ (white arrow), allowing small primary  $\beta$ -grains to form. Heat conduction results in an oriented macrostructure consisting of primary  $\beta$ -grains typical for AM-ed Ti-64.<sup>[10,26,40–43]</sup> The formation of the columnar macrostructure starts within the melt pool and is directed toward the base plate. The heat introduced by the first layers can be quickly dissipated because of the proximity to the base plate. Due to this increased heat dissipation, small, equiaxed primary  $\beta$ -grains form in this lower area. Each additional layer increases the heat input into the underlying material, which leads to heat accumulation. This increased temperature leads to the formation of larger, directionally solidified primary  $\beta$ -grains beginning in the third layer. These macrostructures have to be taken into account for further microstructural analyses. Before going into the microstructural details of the WAAM-ed structure, the development of the base plate and HAZ will be described.

The rolled base plate in **Figure 10d** shows a globular microstructure with coarse  $\alpha$ -grains surrounded by the brighter

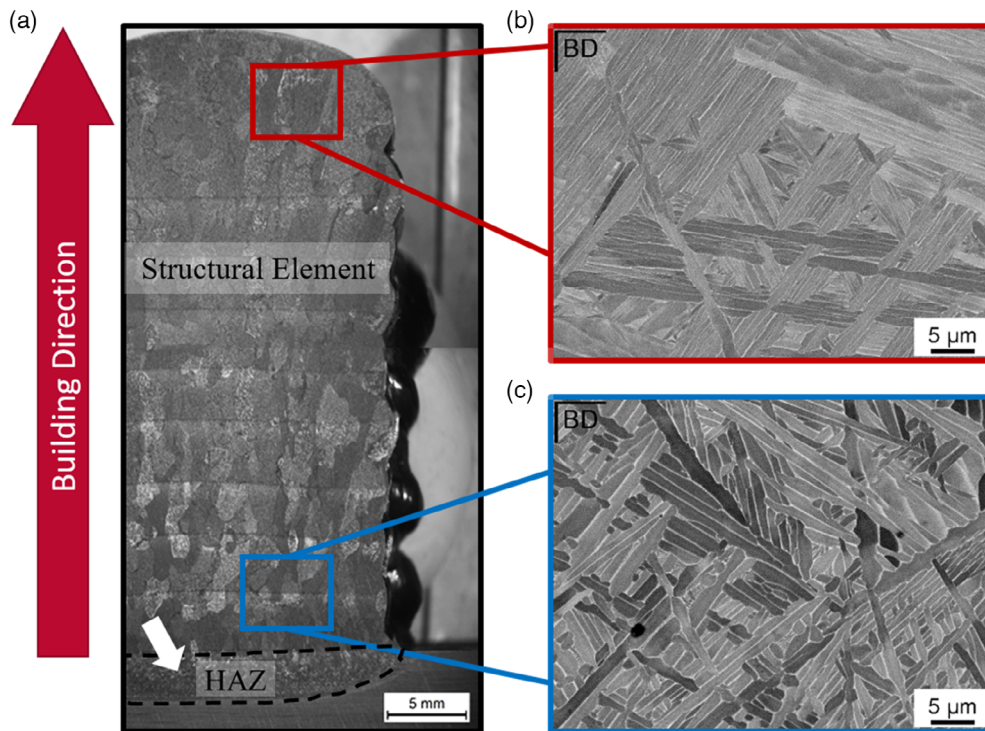


**Figure 9.** a) Macrostructure of an additively manufactured part with the typical corresponding Widmannstätten microstructure in: b) upper layers and c) near the base plate.

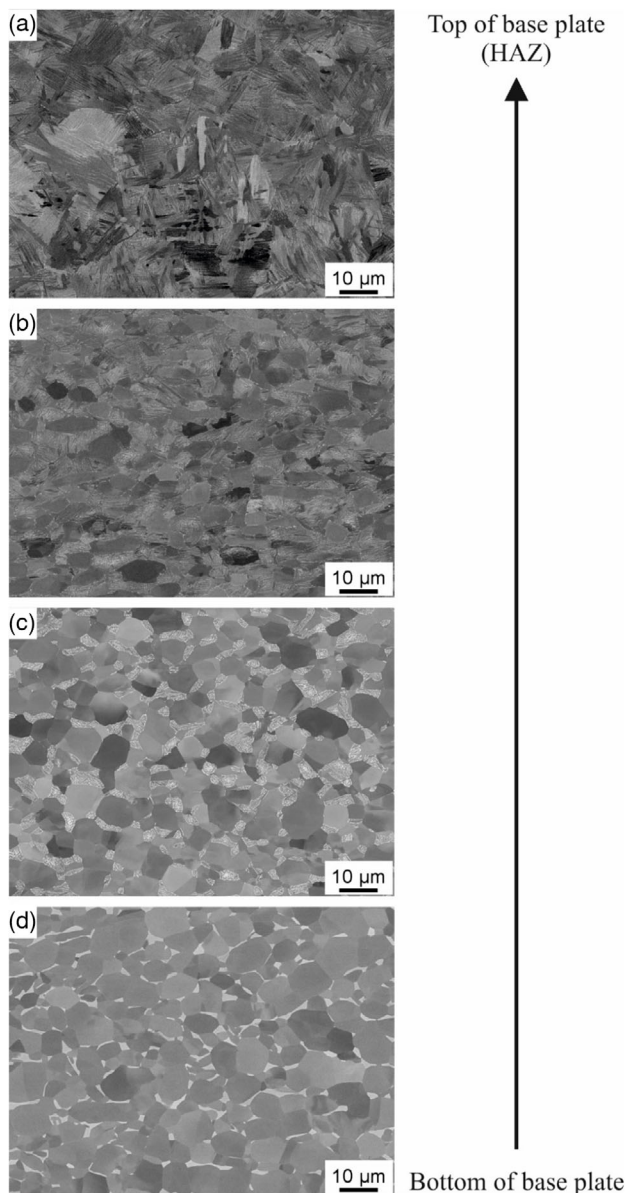


**Figure 10.** Microstructure of the: a) top of the baseplate compared to b–c) the HAZ with decreasing distance (500  $\mu\text{m}$ , each) to the unaffected substrate d).

$\beta$ -phase. In this state, the microstructure consists of 95.3% of  $\alpha$  and 4.7%  $\beta$  phase.

Partial remelting by the welding process leads to the formation of secondary  $\alpha$  lamellae in the  $\beta$  phase. This bimodal microstructure is one of the reasons why additive manufacturing of Ti–64 is so interesting and promising regarding the mechanical properties of the HAZ; see, for example, Åckerfeldt et al.<sup>[44]</sup> With increasing distance to the base plate, the lamellae grow steadily beyond the phase boundaries of the  $\beta$  phase, initially only in favorably oriented phases. From  $\approx 1000 \mu\text{m}$  upward (Figure 10b), this behavior can also be observed in the remaining phases. The phase-composition changes and the amount of  $\alpha$

phase increases slightly to 96.1%. A purely lamellar structure is already evident in the former base plate. The primary  $\beta$  grains are comparatively smaller compared to the upper regions of the specimen. This is due to the transformation of the former columnar microstructure. The prior  $\beta$  grains show a coarsened and oriented growth only at some distance to the HAZ.

In these lower areas of the WAAM-ed specimen, heat can easily be transported toward the base plate, which leads to the conclusion of small lamellar distances caused by rapid cooling. In lower areas, the length of the  $\alpha$  lamellae is also decreased due to smaller prior  $\beta$  grain sizes.

Every additional layer induces a constant heat input which can also be considered intrinsic heat treatment to the lower area of the specimen.<sup>[12]</sup> This intrinsic heat treatment increases lamellar distance, as shown in Figure 9c.

**Figure 11a** reveals the hardness development over the distance to the base plate for the three different linear torch speeds of 66, 82, and 99  $\text{mm min}^{-1}$ . The wire feed speed was kept constant at 6  $\text{m min}^{-1}$ .

The hardness of the 6 mm thick base plate is  $332 \pm 11 \text{ HV}$ . With increasing distance to the bottom of the base plate, the hardness initially decreases up to the HAZ. At a distance of approx. 2.5 mm, first lamellar areas were detected (Figure 10c). In this area, a local hardness minimum of  $318 \pm 10 \text{ HV}$  is present. In the remelted zone, the hardness increases constantly and reaches its maximum of  $344 \pm 18 \text{ HV}$ . In the deposited material, the hardness is constant for higher welding speeds. In contrast to this finding, the hardness constantly decreases for the lowest torch speed. Compared to the single-pass welding tests in Figure 8, it is noticeable that the hardness in the multilayer material has increased. The reason for this can be the recurring intrinsic heat treatment caused by the repeated layer deposition via WAAM. This can reduce the residual stresses, but in contrast, this can also cause coarsening of the lamellae due to the increased heat input, especially as the subsequent layers are applied immediately.

Figure 11b shows the influence of the wire feed speed on the hardness of the WAAM-ed material. In addition, a test in which the welding process was interrupted several times is also shown (checkered bars).

It can be seen that process disturbances such as interruptions have a significant influence on mechanical properties, as they produce different thermal profiles resulting in different microstructures.

The hardness of the continuously produced specimens averages at  $316 \pm 12 \text{ HV}$ . The influence of the  $v_{\text{WFS}}$  and the height seems negligible. This shows the importance of continuous process control and its influence on mechanical properties.

## 9. Heat Treatments

Especially in upper areas of bigger components and for thinner geometries, a supplementary heat treatment is necessary to reduce residual stresses. This is important to further reduce distortion after the final milling. **Figure 12** shows the influence of different heat treatments on the microstructure of specimens built at slow  $v_{\text{TS}}$  in the top row and the high torch speed in

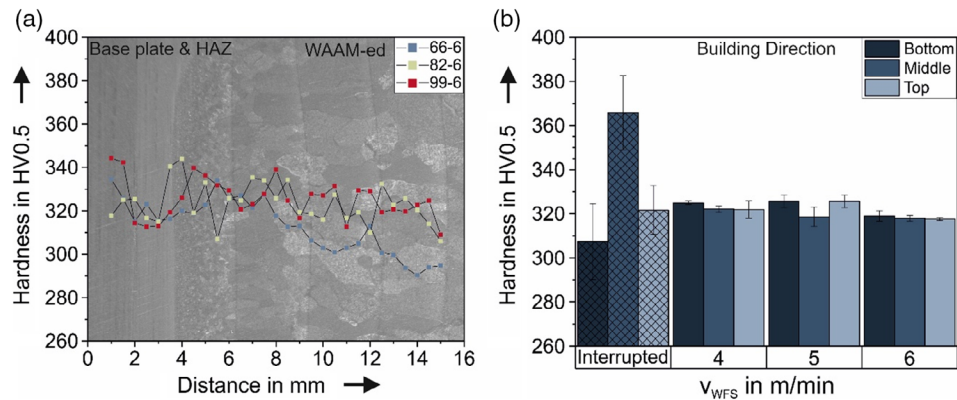


**Figure 11.** Hardness development over the: a) distance to the base plate with constant  $v_{WFS}$  of  $6 \text{ m min}^{-1}$  and b) depending on process management and wire feed speed at a constant  $v_{TS}$  of  $66 \text{ mm min}^{-1}$  for the rest of the WAAM-ed specimen.

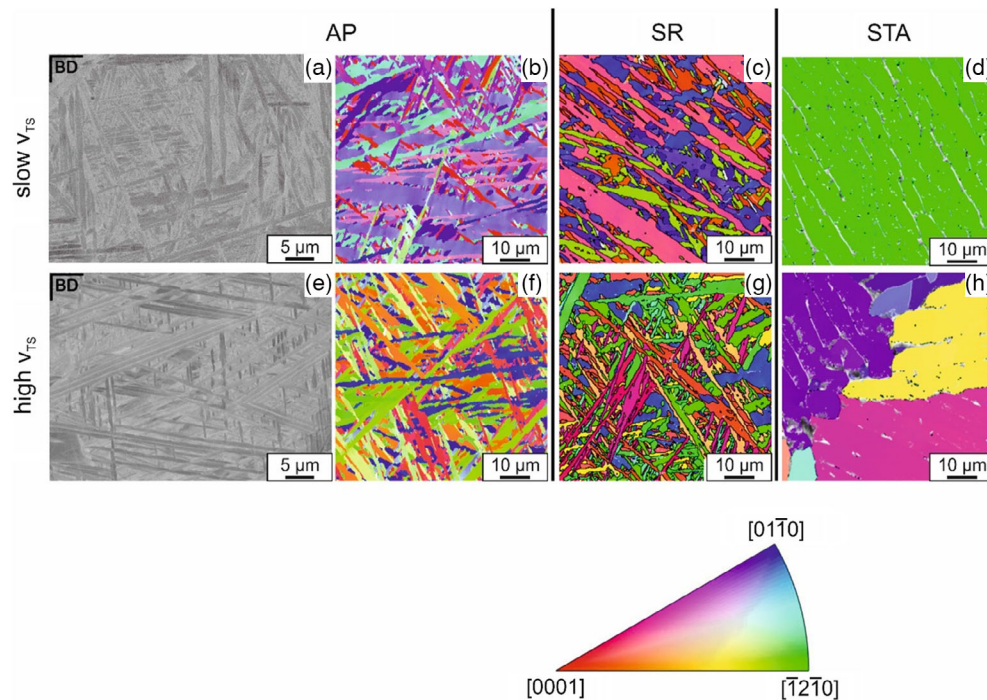


**Figure 12.** Influence of torch speed and heat treatments on microstructure: c,g) stress-relief annealing (SR) and d,h) solution heat treatment and annealing (STA) compared to the AP on microstructure analyzed via a,e) SEM and b,f) EBSD mapping in the building direction.

the bottom row. In the EBSD mapping of the as-printed (AP) and stress-relieved state, it can also be seen that the lamellae distance decreases with increasing torch speed, as shown in Figure 7. Stress relief at  $600 \text{ }^\circ\text{C}$  does not influence the lamellar microstructure of WAAM-ed specimens.

In both states, it can be seen that a statistical distribution of the lamellae orientation prevails regardless of the  $v_{TS}$ . This was also observed in other grains of AP and SR specimens. However, solution treatment and annealing dissolve this structure. Due to the slow cooling from the  $\beta$  region, coarser  $\alpha$  networks with identical orientation form.

Hardness measurements in the building direction of different heat-treated samples are shown in Figure 13. Single-bead specimens in the AP state have a reduced hardness of  $317 \pm 2 \text{ HV}$  produced with slow torch speeds, respectively  $325 \pm 12 \text{ HV}$  for fast  $v_{TS}$ . This slightly increased hardness could be an indication of the higher residual stresses. Although comparable microstructures (Figure 12) have been obtained by SEM analyses, an SR leads to an increase in hardness to  $326 \pm 5 \text{ HV}$  for the slow speed setup and  $349 \pm 7 \text{ HV}$  for the higher torch speed. A possible reason for this behavior could be the formation of finely dispersed  $\alpha''$ -precipitations, see.<sup>[45]</sup> Due to the high cooling rates



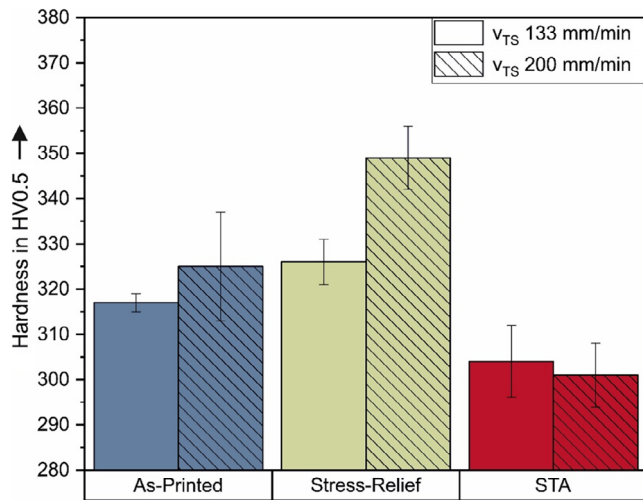


**Figure 13.** Hardness development in dependence on  $v_{TS}$  and the heat treatment.

during additive manufacturing, the supersaturated condition eases the formation of these precipitates. This is also supported by the fact that a higher torch speed leads to a significant increase in hardness compared to slower welding speeds. In contrast, STA heat treatment reduces the hardness by more than

20 HV0.5 compared to the AP state. A reason for that could be the reorientation of the grains during STA, as shown in Figure 12.

## 10. Increasing Complexity

Based on these findings, it can be assumed that in regions facing higher thermal energy inputs caused by the process, such as in T-joints or crossings, an intrinsic local heat treatment is performed, which to some extent may affect the mechanical properties locally.

Therefore, compression test specimens were taken out of the T-joint area. A comparison of these results is shown in Figure 14. Specimens were taken in the building direction in the wall and the T-joint (Figure 14a,c), as well as in the welding direction in the upper and lower regions of the T-joint (Figure 14b,d).

Figure 14a,b compares the mechanical properties of compression tests of the wall (red) with the T-joint area (blue). On the one hand, it can be seen that in the building direction, the parameter adaptation in the crossing point produces comparable mechanical properties. On the other hand, a significant decrease in the welding speed in the T-joint, as by the parameter set 112–11, leads to a decrease in the compressive strength. Consequently, when creating more complex geometries, it is necessary to reduce the velocity in the junction by a maximum of 45% to

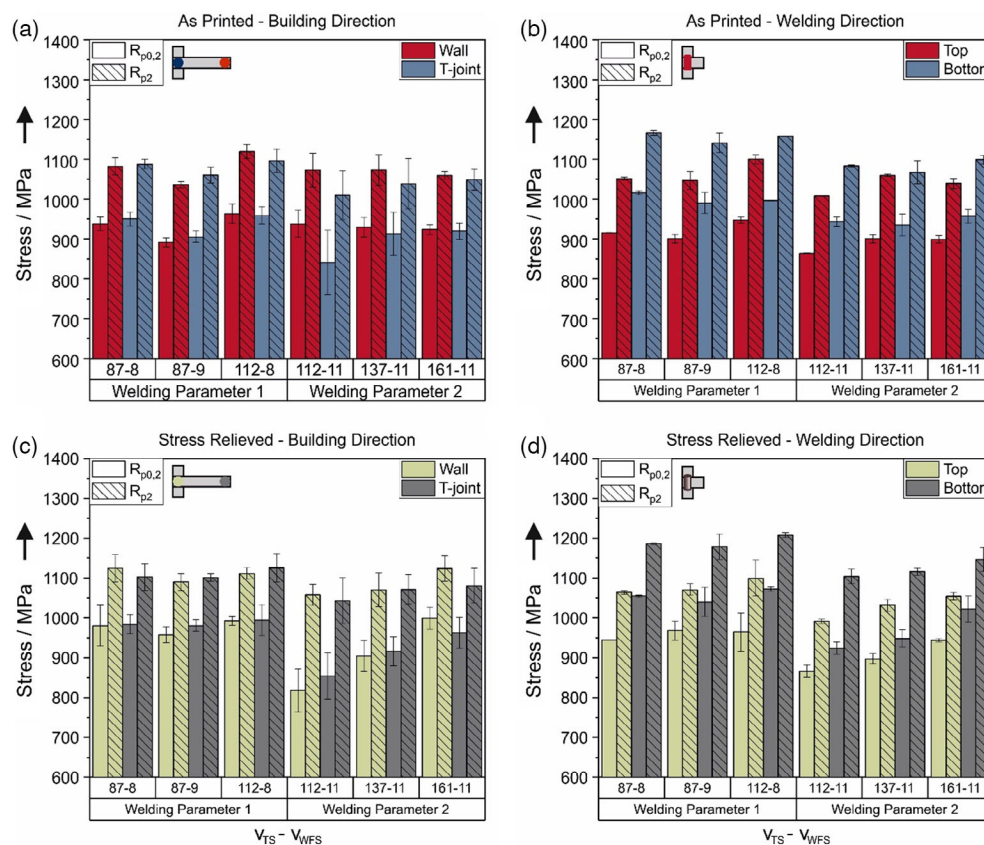


**Figure 14.** Comparison of: a,b) AP state compression tests and c,d) stress-relieved specimens in a,c) building direction, and b,d) welding direction.

produce pore-free and comparable mechanical properties with the commuted wall.

As discussed earlier, heat conduction in the T-joint due to the welding of a wall also occurs along the horizontal direction and is suggested to result in an increased cooling rate. The latest results of another ongoing investigation at TUM also confirm this suggestion.<sup>[46]</sup>

Therefore, the height-dependent mechanical properties will be obtained, especially at lower welding speeds in the T-joint, see Figure 14b. A clear height dependence of the compressive strength of the lower (blue) and upper layers (red) can be seen.

Subsequent stress-relief annealing at 600 °C for 4 h increases the compressive strength for all welding conditions. The height dependence of the mechanical properties decreases but is still visible. For example, the strength of the lower areas of specimens produced by using base parameter 1 with a meander parameter 87.8 is 1055 MPa after 0.2% and 1186 MPa after 2% compression. In the upper layers, the strength drops to 945 and 1064 MPa, respectively.

To explain this behavior, SEM analyses were carried out on already fractured compression specimens.

The comparison of SEM examinations in **Figure 15** reveals that more-extended and less-branched lamellae are present in

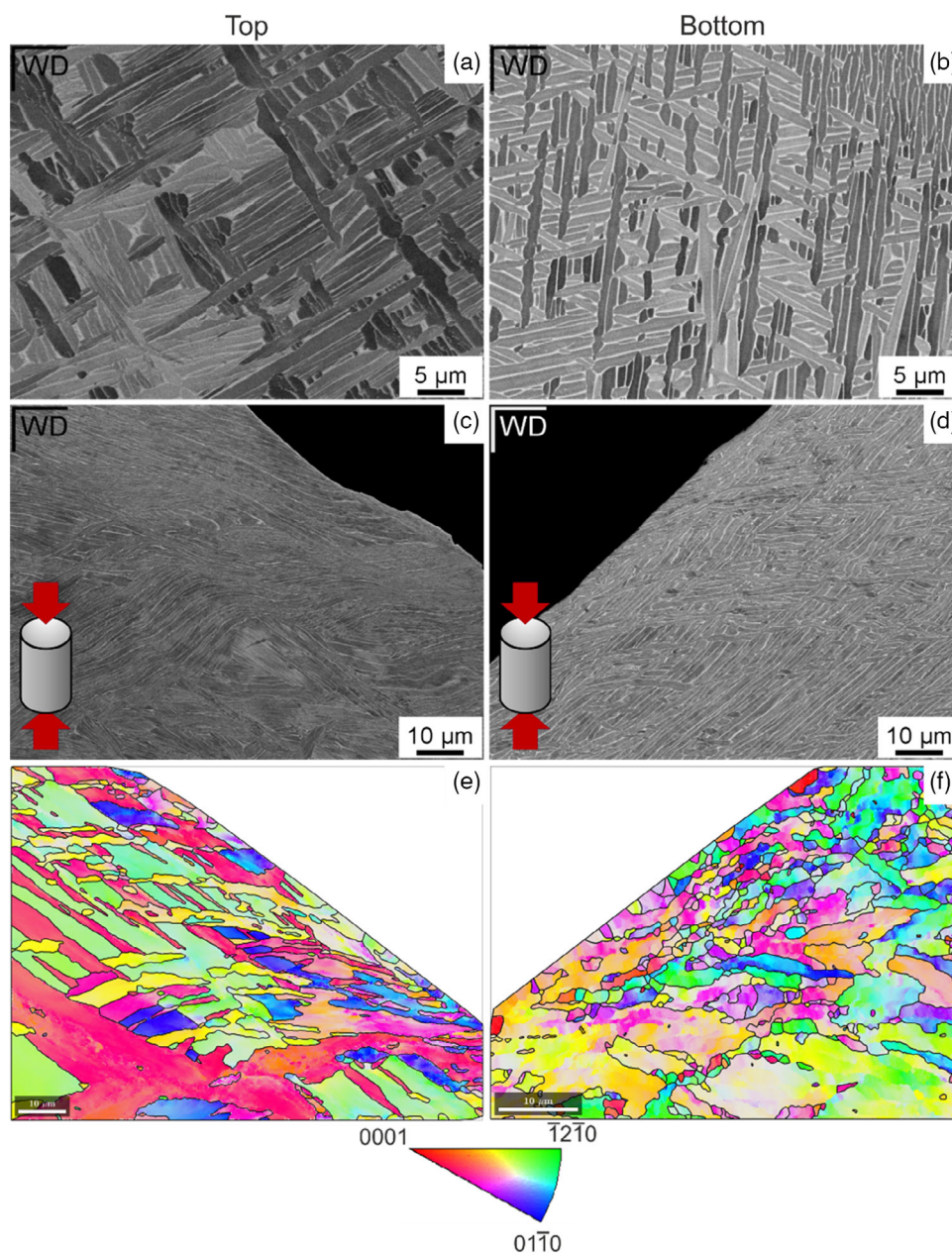


**Figure 15.** Comparison of SEM studies of compression specimens from upper and lower layers: a,b) before compression test, c,d) postmortem and e,f) related EBSD analyses.

the upper regions of the built structure compared to the lower layers. This results from the different cooling rates in the respective areas. Due to the rapid cooling near the base plate, smaller primary  $\beta$  grains can be found. Furthermore, the high cooling rate leads to the formation of basket weave  $\alpha$ .

Therefore, the reduced strengths in the upper areas can be explained by the fact that sliding is facilitated along the longer  $\alpha$  lamellae present in this region. This behavior can be seen in Figure 15c. The EBSD measurement performed in this section illustrates the slippage of the lamellae. This behavior is not seen in lower areas, where shorter lamellae govern the microstructure (Figure 15d and f).

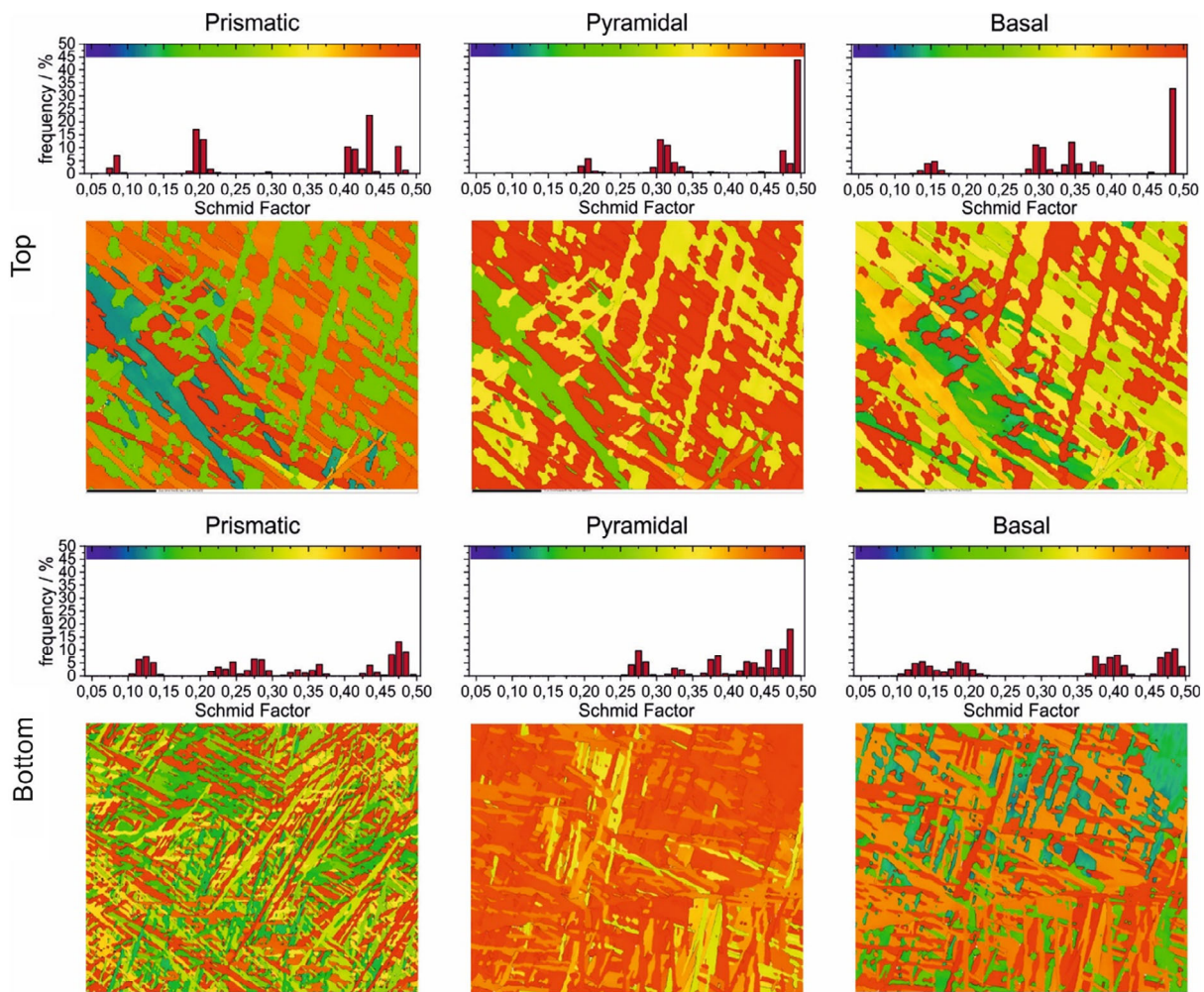
Another reason for the changed sliding behavior may be a change in the Schmid factor and orientation of the lamellae. The height-dependent changes in the Schmid factor were investigated using the EBSD, **Figure 16**. With the help of the Schmid factor, activated slip systems can be determined. Slip systems with a high Schmid factor are the first to reach the critical shear stress, thus contributing to the deformation.

Figure 16 compares the prismatic, pyramidal, and basal slip systems of the upper and lower parts of the wall. Especially for the prismatic and basal slip systems, it can be seen that the frequency of ideally oriented regions with a Schmid factor of 0.5 has decreased compared to the upper regions. Thus, increased shear stress is needed to initiate plastic deformation in these areas. This results in increased yield strength and 0.2% compression strength.

The increased frequency of the higher Schmid factors of the pyramidal  $\{1011\}1210$ , but also of the basal  $\{1011\}1210$  system at the top of the weld, indicates that the critical shear stress is reached more easily, and thus, a lower strength is obtained in these regions, see Figure 14b.

Furthermore, a change in the orientation of the lamellae can be seen in the EBSD images. While in the lower area each lamella is oriented differently, adjacent lamellae near the upper end of the weld show the same orientation.

It can be seen that because of the intrinsic heat treatment and the different thermodynamic states, WAAM-ed parts lead to complex microstructure and thus height-dependent



**Figure 16.** The EBSD analysis to determine the influence of height on the Schmid factor in the loading direction for the prismatic (left), pyramidal (center), and basal slip systems (right).

mechanical properties. The reason for that could be the constant interlayer time during manufacturing. Heat can build-up with each layer due to the poor thermal conductivity of titanium. The change of the Schmid factor in combination with the hard  $\alpha$  phase surrounded by more ductile  $\beta$  is one of the reasons for the different deformation behavior in the upper layers of the weld. The microstructural change from basket weave to lamellar  $\alpha$  within a specimen also might contribute to the decrease in strength.

A promising way to solve this problem is to consider the interlayer temperature rather than the time between the layer depositions. By controlling the temperature of the seam to be welded onto, the cooling conditions of the additively manufactured areas can be kept more constant. This work also revealed the complexity of parameter upscaling from smaller to bigger and from simple to more complex parts. It has turned out that the  $v_{TS}$  needs to be decreased in the feeding direction to minimize splatter and maximize the interlayer welding connection. The increased energy input made it possible to sustainably exclude pores and increase the weld pool width according to Section 3.

## 11. Summary and Conclusions

The microstructural evolution of Ti-64 was studied throughout the WAAM process chain. First, single-layer material was welded and examined for dimensional stability, alloy burn-off, and the influence of different process gases. It was found that a minimal reduction of the Al concentration occurred, and the geometry was strongly dependent on the selected welding speed. Furthermore, it was shown that the helium could stabilize the arc, however, the process window is minimized. The study of the influence of the welding process showed that the CMT process significantly minimized distortion and spattering.

The transfer of the process parameters identified in the single-layer test to a pendulum, and multilayer walls have shown that it is essential to adapt them to the new geometry to avoid further spattering and pores. SEM investigations revealed a height-dependent microstructure with basket weave  $\alpha$  in the lower parts and lamellar structure in the upper regions. In addition, the HAZ was investigated in more detail. Microstructurally, a globular structure is present up to the HAZ.

At a close distance to the HAZ, lamellar  $\alpha$  forms in the  $\beta$  phase. With increasing distance, lamellar  $\alpha$  outgrows the  $\alpha$ -grain boundaries. This bimodal structure of the HAZ shows good mechanical properties and is comparable to the AP WAAM-ed material. Subsequent heat treatment in the form of stress-relief annealing at 600 °C for 4 h increased the overall mechanical properties, as this relieved the residual stresses introduced during the welding process.

It was found that the pyramidal slip system was preferred in upper areas of the WAAM-ed material. However, the preferred slip systems change toward lower regions. This difference, in combination with the microstructural change, increases the strength in the lower areas despite larger  $\alpha$ -laths. Postmortem analyses have also shown that sliding is facilitated along the longer  $\alpha$  lamellae surrounded by ductile  $\beta$  phase in the upper regions of the weld. A reason for that was found to be the

microstructural changes in combination with an adaptation of the Schmid factor.

Regarding scalability, the process parameters for multilayer, pendulum, and complex seams need to be adjusted accordingly.

The results clearly show that by the WAAM process and the described parameters, it is feasible to achieve the mechanical properties of standard rolled Ti-64. Another advantage is eliminating further processing steps, such as hot isostatic pressing. In contrast to laser powder bed fusion or electron beam welding processes, it is also possible to produce at higher build-up rates and to map significantly larger geometries.

Therefore, further investigations should focus on the thermal household and constant interlayer temperatures of the WAAM-ed Ti-64 to decrease the height dependency of the microstructure and the mechanical properties.

## Acknowledgements

The authors would like to acknowledge the Federal Ministry for Economic Affairs and Climate Action (BMWK) for providing financial assistance and funding for the research project REGULUS (grant number 20W1709D) and the supervision of the German Aerospace Center e. V. Furthermore the authors would like to acknowledge Max Bader and Florens Bach for their support during the research work and for performing heat treatments. The authors would also like to acknowledge the REGULUS project partners AMAG components Übersee GmbH, HEGGEMANN AG, and Software Factory GmbH for fruitful discussions evaluating the results. This paper has been corrected September 20, 2022 after initial online publication.

Open Access funding enabled and organized by Projekt DEAL.

## Conflict of Interest

The authors declare no conflict of interest.

## Data Availability Statement

The data that support the findings of this study are available from the corresponding author upon reasonable request.

## Keywords

additive manufacturing, alpha-beta alloys, heat treatments, mechanical properties, microstructures, Ti-64, WAAM

Received: July 15, 2022

Revised: August 30, 2022

Published online: September 18, 2022

- [1] C. Cui, B. Hu, L. Zhao, S. Liu, *Mater. Des.* **2011**, 32, 1684.
- [2] R. R. Boyer, *Mater. Sci. Eng., A* **1996**, 213, 103.
- [3] B. Callegari, J. P. Oliveira, K. Aristizabal, R. S. Coelho, P. P. Brito, L. Wu, N. Schell, F. A. Soldera, F. Mücklich, H. C. Pinto, *Mater. Charact.* **2020**, 165, 110400.
- [4] C. A. F. Salvador, E. L. Maia, F. H. Costa, J. D. Escobar, J. P. Oliveira, *Sci. Data.* **2022**, 9, 188.
- [5] G. Lütjering, J. C. Williams, *Titanium*, 2nd ed., Springer, Berlin; New York, NY **2007**.
- [6] J. Allen, *An Investigation into the Comparative Costs of Additive Manufacture vs. Machine From Solid for Aero Engine Parts*, Meeting

- Proceedings RTO-MP-AVT-139, Paper 17, RTO, Neuilly-sur-Seine, France **2006**, pp. 17-1–17-10, <http://www.rto.nato.int/abstracts.asp>.
- [7] R. R. Boyer, *JOM* **2010**, 62, 21.
- [8] M. S. Kalienko, M. O. Leder, A. V. Volkov, A. V. Zhelnina, P. E. Panfilov, *Russ. Metall. Met.* **2020**, 2020, 325.
- [9] D. P. Satko, J. B. Shaffer, J. S. Tiley, S. L. Semiatin, A. L. Pilchak, S. R. Kalidindi, Y. Kosaka, M. G. Glavicic, A. A. Salem, *Acta Mater.* **2016**, 107, 377.
- [10] R. Gaddam, B. Sefer, R. Pederson, M.-L. Antti, *IOP Conf. Ser. Mater. Sci. Eng.* **2013**, 48, 012002.
- [11] R. Gaddam, B. Sefer, R. Pederson, M.-L. Antti, *Mater. Charact.* **2015**, 99, 166.
- [12] F. Wang, S. Williams, P. Colegrove, A. A. Antonysamy, *Metall. Mater. Trans. A* **2013**, 44, 968.
- [13] S. M. Kelly, S. L. Kampe, *Metall. Mater. Trans. A* **2004**, 35, 1861.
- [14] P. A. Kobryn, N. R. Ontko, L. P. Perkins, J. S. Tiley, *Additive Manufacturing of Aerospace Alloys For Aircraft Structures*, Meeting Proceedings RTO-MP-AVT-139, Paper 3, RTO, Neuilly-sur-Seine, France **2006**, pp. 3-1–3-10, <http://www.rto.nato.int/abstracts.asp> **2006**. <https://apps.dtic.mil/sti/citations/ADA521726> (accessed: April 2021).
- [15] E. Brandl, A. Schoberth, C. Leyens, *Mater. Sci. Eng., A* **2012**, 532, 295.
- [16] F. Martina, J. Mehnen, S. W. Williams, P. Colegrove, F. Wang, *J. Mater. Process. Technol.* **2012**, 212, 1377.
- [17] C. Fuchs, D. Baier, D. Elitzer, R. Kleinwort, A. Bachmann, M. F. Zäh, *Z. Wirtsch. Fabrikbetr.* **2019**, 114, 431.
- [18] D. Baier, A. Bachmann, M. F. Zaeh, *Procedia CIRP* **2020**, 95, 54.
- [19] D. Weger, D. Baier, A. Straßer, S. Prottung, T. Kränkel, A. Bachmann, C. Gehlen, M. Zäh, in *Second RILEM Int. Conf. Concrete and Digital Fabrication* (Eds: F. P. Bos, S. S. Lucas, R. J. M. Wolfs, T. A. M. Salet), Springer Inter. Publishing, Cham **2020**, pp. 978–987.
- [20] A. Förner, S. Giese, C. Arnold, P. Felfer, C. Körner, S. Neumeier, M. Göken, *Sci. Rep.* **2020**, 10, 15153.
- [21] B. Diepold, N. Vorlauffer, S. Neumeier, T. Gartner, M. Göken, *Int. J. Miner. Metall. Mater.* **2020**, 27, 640.
- [22] J.-P. Kruth, M. C. Leu, T. Nakagawa, *CIRP Ann.* **1998**, 47, 525.
- [23] B. Baufeld, E. Brandl, O. van der Biest, *J. Mater. Process. Technol.* **2011**, 211, 1146.
- [24] S. W. Williams, F. Martina, A. C. Addison, J. Ding, G. Pardal, P. Colegrove, *Mater. Sci. Technol.* **2016**, 32, 641.
- [25] W. C. Ke, J. P. Oliveira, B. Q. Cong, S. S. Ao, Z. W. Qi, B. Peng, Z. Zeng, *Addit. Manuf.* **2022**, 50, 102513.
- [26] A. Ramalho, T. G. Santos, B. Bevans, Z. Smoqi, P. Rao, J. P. Oliveira, *Addit. Manuf.* **2022**, 51, 102585.
- [27] S. Li, J. Y. Li, Z. W. Jiang, Y. Cheng, Y. Z. Li, S. Tang, J. Z. Leng, H. X. Chen, Y. Zou, Y. H. Zhao, J. P. Oliveira, Y. Zhang, K. H. Wang, *Addit. Manuf.* **2022**, 57, 102958.
- [28] A. E. Davis, A. Caballero, P. B. Prangnell, *Materialia* **2020**, 13, 100857.
- [29] J. Donoghue, A. E. Davis, C. S. Daniel, A. Garner, F. Martina, J. Quinta da Fonseca, P. B. Prangnell, *Acta Mater.* **2020**, 186, 229.
- [30] D. Lunt, A. Ho, A. Davis, F. Martina, J. Hönnige, J. Q. da Fonseca, P. Prangnell, *MATEC Web Conf.* **2020**, 321, 03008.
- [31] A. Ho, H. Zhao, J. W. Fellowes, F. Martina, A. E. Davis, P. B. Prangnell, *Acta Mater.* **2019**, 166, 306.
- [32] M. Neikter, P. Åkerfeldt, R. Pederson, M.-L. Antti, V. Sandell, *Mater. Charact.* **2018**, 143, 68.
- [33] M. Neikter, *IOP Conf. Ser. Mater. Sci. Eng.* **2017**, 258, 012007.
- [34] J. B. Chu, *Thesis*, Massachusetts Institute of Technology **2020**. <https://dspace.mit.edu/handle/1721.1/126954> (accessed: July 2021).
- [35] S. Selvi, A. Vishvakshnan, E. Rajasekar, *Def. Technol.* **2018**, 14, 28.
- [36] C. G. Pickin, K. Young, *Sci. Technol. Weld. Joining* **2006**, 11, 583.
- [37] K. Wei, Z. Wang, X. Zeng, *Mater. Lett.* **2015**, 156, 187.
- [38] T. DebRoy, H. L. Wei, J. S. Zuback, T. Mukherjee, J. W. Elmer, J. O. Milewski, A. M. Beese, A. Wilson-Heid, A. De, W. Zhang, *Prog. Mater. Sci.* **2018**, 92, 112.
- [39] J. Yin, W. Zhang, L. Ke, H. Wei, D. Wang, L. Yang, H. Zhu, P. Dong, G. Wang, X. Zeng, *Int. J. Mach. Tools Manuf.* **2021**, 161, 103686.
- [40] B. E. Carroll, T. A. Palmer, A. M. Beese, *Acta Mater.* **2015**, 87, 309.
- [41] P. Åkerfeldt, M.-L. Antti, R. Pederson, *Mater. Sci. Eng., A* **2016**, 674, 428.
- [42] M. Benedetti, V. Fontanari, M. Bandini, F. Zanini, S. Carmignato, *Int. J. Fatigue* **2018**, 107, 96.
- [43] G. Kasperovich, J. Hausmann, *J. Mater. Process. Technol.* **2015**, 220, 202.
- [44] P. Åkerfeldt, R. Pederson, M.-L. Antti, *Microstructure and Mechanical Properties of Laser Metal Deposited Ti-6Al-4V*, Social Sciences Academic Press, China **2012**, pp. 1730–1734. <http://urn.kb.se/resolve?urn=urn:nbn:se:ltu:diva-31848> (accessed: February 2021).
- [45] M. I. Utama, N. Park, E. R. Baek, *Met. Mater. Int.* **2019**, 25, 439.
- [46] C. Fuchs, D. Elitzer, H. W. Höppel, M. Göken, M. F. Zaeh, *J. Manuf. Mater. Process.* **2022**, 6, unpublished.